



Final Draft **of the original manuscript**

Jäger, N.; Meindlhumer, M.; Spor, S.; Hruby, H.; Julin, J.; Stark, A.; Nahif, F.; Keckes, J.; Mitterer, C.; Daniel, R.:

Microstructural evolution and thermal stability of AlCr(Si)N hard coatings revealed by in-situ high-temperature high-energy grazing incidence transmission X-ray diffraction.

In: Acta Materialia. Vol. 186 (2020) 545 - 554.

First published online by Elsevier: 18.01.2020

<https://dx.doi.org/10.1016/j.actamat.2020.01.026>

Microstructural evolution and thermal stability of AlCr(Si)N hard coatings revealed by in-situ high-temperature high-energy grazing incidence transmission X-ray diffraction

N. Jäger^a, M. Meindlhumer^a, S. Spor^{a,b}, H. Hruby^b, J. Julin^c, A. Stark^d, F. Nahif^b, J. Keckes^{e,f}, C. Mitterer^f, R. Daniel^a

^aChristian Doppler Laboratory for Advanced Synthesis of Novel Multifunctional Coatings at the Department of Materials Science, Montanuniversität Leoben, Austria

^bvoestalpine eifeler Vacotec GmbH, Düsseldorf, Germany

^cInstitute of Ion Beam Physics and Materials Research at the Helmholtz-Zentrum Dresden-Rossendorf, Dresden, Germany

^dHelmholtz Zentrum Geesthacht, Centre for Materials and Coastal Research, Geesthacht, Germany

^eErich Schmid Institute for Materials Science, Austrian Academy of Sciences, Austria

^fDepartment of Materials Science, Montanuniversität Leoben, Austria

Abstract

An extensive understanding about the microstructural evolution and thermal stability of the metastable AlCr(Si)N coating system is of considerable importance for applications facing high temperatures, but it is also a challenging task since several superimposed processes simultaneously occur at elevated temperatures. In this work, three AlCr(Si)N coatings with 0 at.%, 2.5 at.% and 5 at.% Si were investigated by in-situ high-temperature high-energy grazing incidence transmission X-ray diffraction (HT-HE-GIT-XRD) and complementary differential scanning calorimetry and thermogravimetric analysis measurements combined with conventional ex-situ X-ray diffraction. The results revealed (i) a change in the microstructure from columnar to a fine-grained nano-composite, (ii) a reduced decomposition rate of CrN to Cr₂N, also shifted to higher onset temperatures from ~ 1000 °C to above 1100 °C and (iii) an increase of lattice defects and micro strains resulting in a significant increase of compressive residual strain with increasing Si content. While the Si-containing coatings in the as-deposited state show a lower hardness of 28 GPa compared to AlCrN with 32 GPa, vacuum annealing at 1100 °C led to an increase in hardness to 29 GPa for the coatings containing Si and a decrease in hardness to 26 GPa for AlCrN. Furthermore, the in-situ HT-HE-GIT-XRD method allowed for simultaneously accessing temperature-dependent variations of the coating microstructure (defect density, grain size), residual strain state and phase stability up to 1100 °C. Finally, the results established a deeper understanding about the relationships between the elemental composition of the materials, the resulting microstructure including crystallographic phases and residual strain state, and the coating properties from room temperature up to 1100 °C.

Keywords: AlCrSiN, nano-composite, cathodic arc, thermal stability,

1. Introduction

Transition metal nitrides find widespread use as hard protective coatings in applications with surfaces exposed to wear. The rising demand on wear-protective hard coatings for severe applications has stimulated the development of advanced coatings with sophisticated microstructural and compositional design [1–5]. Besides substantial requirements on mechanical properties, also thermal stability and oxidation resistance of such materials play a key role in modern high-temperature applications like dry cutting or high speed cutting. The temperatures of cutting tools operating under harsh conditions may exceed 1000 °C [6], especially near to the cutting edge. Nowadays, ternary metal nitride coatings such as AlCrN are frequently used in industry [7, 8] due to their high hardness, wear and oxidation resistance [9–11]. The AlCrN system can be synthesized with face-centered cubic structure up to an Al content of 75 at.% on the metal sublattice [12]. By exceeding this critical solubility limit, an additional phase with hexagonal crystallographic structure forms, becoming dominant at higher Al contents [13]. Since cubic (c-)AlCrN is a thermodynamically

metastable solid solution, hexagonal (h-)Al(Cr)N forms at elevated temperatures and the CrN-enriched matrix decomposes in a two-step reaction into Cr₂N and finally Cr [14]. Especially the decomposition into Cr₂N is highly undesirable, as the associated release of N₂ yields a porous structure and deteriorates mechanical properties.

One approach to further improve the performance of hard coatings is to enhance the material's properties by alloying. A promising candidate as alloying element in AlCrN coatings is Si, as shown by several successful attempts enhancing the mechanical properties, the behaviour at high-temperatures and the tribological performance of AlCrN by adding Si [15–17]. Since the solubility limit of Si in AlCrN is low [18], Si tends to segregate along grain boundaries where it forms an additional amorphous (a-)Si_xN_y phase [19–21]. A typical MeN/a-Si_xN_y (Me = Al/Cr) nano-composite structure is formed [22, 23], composed of crystallites embedded in an amorphous tissue, which results in a material with completely new properties. Benefits may arise from the nano-composite hardening effect, where dislocation movement is hindered at grain boundaries and at the interface with the a-Si_xN_y tissue [24], or by suppressed inter-

granular diffusion and thus restricted propagation of oxidation [20].

While AlCr(Si)N coating systems in various compositions have been investigated in terms of microstructure [15, 18], mechanical [17] and tribological [25] properties or cutting performance [23, 26], a detailed study of the thermal stability is still missing. In this work, the influence of Si content on the thermal stability of three AlCr(Si)N coatings with a fixed Al/Cr atomic ratio of 70/30 and 0 at.%, 2.5 at.% and 5 at.% Si, respectively, is studied. The recently developed approach [27, 28] using in-situ high-temperature high-energy grazing-incidence transmission X-ray diffraction (HT-HE-GIT-XRD) at the German Synchrotron (DESY) at PETRA III was used to analyse the coatings. This method relies on a cross-sectional approach investigating the coating-substrate system in transmission geometry, providing simultaneously access to temperature-dependent variations of the coating microstructure (defect density, grain size), residual strain state, thermal expansion coefficients of coating and substrate material and phase stability. Complementary differential scanning calorimetry (DSC) and thermogravimetric analysis (TGA) measurements combined with conventional ex-situ X-ray diffraction were performed on powdered coatings to determine structural changes occurring at elevated temperatures up to 1450 °C.

The results reveal a fundamental change in microstructure and thus material's properties when Si is added to the AlCrN system. A considerably grain refinement is observed for the coatings containing Si, originating from the formation of a nanocomposite structure. Additionally, Si reduces the solubility limit of AlN in CrN, resulting in a purely cubic-phased AlCrN coating and a dual-phase (hexagonal and cubic) microstructure of the AlCrSiN coatings. The in-situ HT-HE-GIT-XRD measurements reveal a shift of the decomposition (CrN into Cr₂N and N₂) to higher temperatures from 1050 °C to slightly below 1100 °C for AlCrN and AlCrSi_{2.5}N, respectively, and a totally suppressed Cr₂N formation for AlCrSi₅N up to the maximum applied temperature of 1100 °C. Furthermore, the development of defect density, grain size and residual strains as a function of temperature is evaluated. Complementary DSC and TG measurements confirm this positive influence of Si, demonstrated by a retarded onset of Cr₂N formation from 950 °C in the case of Si-free AlCrN to 1080 °C with increasing Si content. Above 1200 °C, the N₂ aggravates, which results in the formation of pure Cr and Cr₃Si in the case of the Si containing coatings. The in-situ HT-HE-GIT-XRD approach and complementary DSC/TG analysis of the investigated AlCr(Si)N coating-systems reveal the influence of Si on microstructure, phase composition and thermal stability and allow for a comprehensive understanding of the underlying structure-stress-property relations.

2. Experimental methods

2.1. Film deposition

For this study three AlCr(Si)N coatings with varying Si-content and a fixed Al/Cr atomic ratio of 70/30 were deposited

by cathodic arc evaporation using an industrial-sized coating system (alpha400P, voestalpine eifeler Vacotec) equipped with sets of six Al₇₀Cr₃₀, Al_{66.5}Cr_{28.5}Si₅ and Al₆₃Cr₂₇Si₁₀ cathodes, respectively. The coatings were grown on mirror-polished cemented carbide substrates (WC, 6 wt.% Co) and on mild steel foil. Prior to deposition, the substrates were plasma-etched to remove all contaminants and to activate the surface for better adhesion. The substrate temperature of 480 °C, the arc current on each cathode of 100 A and the N₂ pressure of 4 Pa were kept constant during deposition. A substrate bias voltage of -100 V was applied and onefold planetary substrate rotation with 2 min⁻¹ was used.

2.2. Film characterisation

Fracture cross-sections of the coatings were investigated in terms of coating thickness and morphology using a Zeiss Leo1525 scanning electron microscope (SEM). The elemental composition of the coatings was measured by Elastic Recoil Detection Analysis (ERDA) in an area of approximately 1.5 mm × 1.5 mm per sample using a 43 MeV ³⁵Cl⁷⁺ ion beam. The angle between the sample normal and the incoming beam was 75°, the scattering angle was 31° and the recoiling ions were detected using a Bragg Ionization Chamber.

DSC and TG measurements of the coatings were performed using a Setaram Setsys Evo 2400 system. To obtain a sufficient DSC signal from the coatings without an influence of the substrate material, the steel foil was removed chemically in 10 % nitric acid. After filtering and washing with ethanol, the remaining coating material was ground in an agate mortar to obtain a fine powder. At first, 20 mg of each powdered sample was heated in Ar atmosphere up to 1450 °C using a heating rate of 20 K min⁻¹ and cooled down at a cooling rate of 50 K min⁻¹ after an isothermal holding time of 30 min. Each run was performed two times under the same conditions and the second run served as a baseline. Additionally, further powder samples (20 mg each) were annealed up to 520 °C, 850 °C, 950 °C, 1000 °C, 1080 °C, 1200 °C, 1280 °C and 1360 °C, respectively. All annealed powders were investigated using a Bruker D8 Advance diffractometer equipped with an energy-dispersive Sol-X detector and applying Cu-K α radiation (8.04 keV). The comparison of XRD data of the samples annealed at various temperatures with the DSC and TG measurements allowed for a better understanding of the different partially overlapping reactions during annealing.

A detailed in-situ analysis of microstructure and strain state as a function of temperature was performed at the German Electron Synchrotron (DESY) at PETRA III, beamline P07B. An X-ray energy of 87.1 keV and a pencil-like shaped beam with a size of 400 μ m × 100 μ m allowed for measuring the entire coating-substrate system in transmission geometry, using rectangular blocked cemented carbide samples with a size of 10 mm × 5 mm × 5 mm and a coating thickness > 11 μ m. The annealing was performed in vacuum with a total pressure of 2 Pa to avoid oxidation during heating, using a dilatometer Bähr DIL 805. The samples were heated up to 1100 °C at a heating rate of 1 K s⁻¹ and cooled down to room temperature (RT) by an Ar flow with a cooling rate of 1 K s⁻¹ after a holding

segment of 300 s at maximum temperature. The actual temperature during the experiment was recorded using a thermocouple brazed to the sample surface. A two-dimensional Perkin-Elmer detector with a pixel size of $200\ \mu\text{m}^2$, positioned at a distance of 1950 mm behind the samples, collected Debye-Scherrer diffraction frames at each temperature step. The detector was calibrated using LaB₆-powder and the software package Fit2D [29]. The evaluation of the measurements of the coatings was performed using a pyFAI software package [30]. For more information about the method and a detailed description of the data evaluation see [28].

Hardness and elastic modulus of the coatings were determined by nanoindentation using an ultra-micro indentation system (UMIS, Fischer-Cripps Laboratories) equipped with a Berkovich diamond tip. To get a sufficient surface quality for the indentation experiments, the samples were locally mechanically polished. The load-displacement curves were recorded under thermal equilibrium to avoid the effect of thermal drift. The indentations were performed in the load controlled mode in the range from 10 mN to 30 mN and the average values were evaluated according to the Oliver and Pharr method [31].

The coated samples used for nanoindentation measurements and as fracture cross-sections of the annealed state were annealed at 1100 °C for 30 min in an HTM Reetz vacuum furnace.

3. Results

3.1. Elemental composition

The elemental composition of the coatings obtained by ERDA is presented in Table 1. The measurements reveal nearly stoichiometric nitrides and a slight loss of Al during deposition compared to the initial cathode composition ($Al/Cr = 2.3$) due to preferred gas scattering of the lighter Al atoms in the plasma discharge during deposition [15]. The Si content of the coatings corresponds to the composition of the particular cathodes. The oxygen contamination of all coatings is ≤ 0.4 at.%. For simplicity, the coatings are denoted as AlCrN, AlCrSi_{2.5}N and AlCrSi₅N throughout the paper, corresponding to the used Al₇₀Cr₃₀, Al_{66.5}Cr_{28.5}Si₅ and Al₆₃Cr₂₇Si₁₀ cathodes, respectively.

Table 1: Elemental composition of the coatings obtained by ERDA.

Cathode composition	Coating composition [at. %]				
	Al	Cr	Si	N	Al/Cr
Al ₇₀ Cr ₃₀	32.6	16.0	0	51.0	2.0
Al _{66.5} Cr _{28.5} Si ₅	32.6	14.0	2.6	50.6	2.3
Al ₆₃ Cr ₂₇ Si ₁₀	30.8	13.7	4.7	50.5	2.2

3.2. Coating morphology and microstructure

SEM micrographs of fracture cross-sections of the coatings in the as-deposited state of the samples and after vacuum annealing at 1100 °C for 30 min are shown in Figure 1. The

coating thickness is 11 μm , 11.8 μm and 12.8 μm for AlCrN, AlCrSi_{2.5}N and AlCrSi₅N, respectively, revealing an increasing deposition rate with increasing Si content in the cathodes. While the AlCrN coating without Si (Figure 1a) exhibits coarse columnar grains, the morphology transforms towards a more glassy and featureless structure with increasing Si content (Figure 1b,c), which is an indication for the formation of a fine-grained nano-composite structure [17, 22]. After vacuum annealing at 1100 °C for 30 min, the coating microstructure of AlCrN in Figure 1d appears to be slightly coarser grained, while it remains glassy and featureless for the Si-containing coatings in Figure 1e and f.

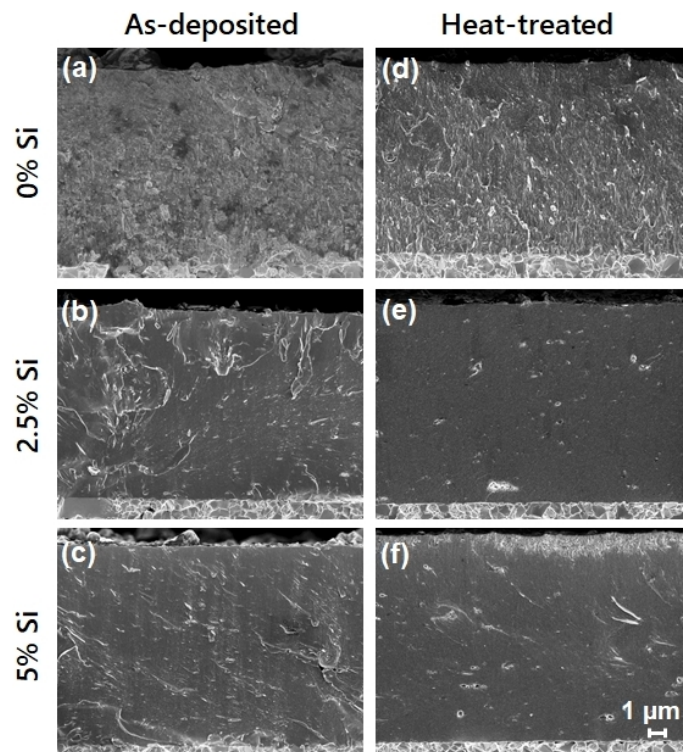


Figure 1: SEM micrographs of fracture cross-sections of (a and d) AlCrN, (b and e) AlCrSi_{2.5}N and (c and f) AlCrSi₅N on cemented carbide substrates in the (a-c) as-deposited state and (d-f) after annealing at 1100 °C.

3.3. Thermal stability

3.3.1. DSC and TG measurements of powdered samples

Figure 2 shows the heat flow and the corresponding mass change of the AlCr(Si)N coatings as a function of annealing temperature. The variations in the heat-flow curves indicate that various reactions occur during annealing, corresponding to diffusion-driven structural changes, reflected also by changes of the sample mass. The superimposed signal in relatively small temperature ranges suggests a variety of structural changes, which occur almost simultaneously. In order to better understand the changes, XRD analysis of powders was performed after various annealing steps at temperatures indicated by vertical lines in Figure 2. The obtained X-ray diffractograms are presented in Figure 3.

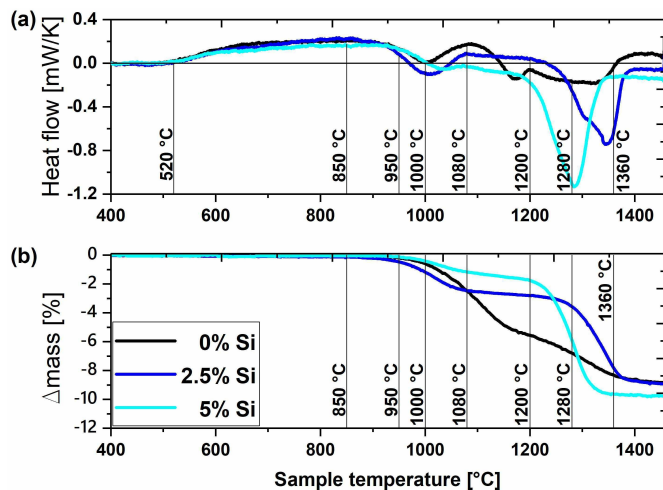


Figure 2: (a) DSC and (b) TG curves of AlCrN, AlCrSi_{2.5}N and AlCrSi₅N in Ar atmosphere. Annealing temperatures for ex-situ XRD measurements of powders are inserted.

The formation of a nano-composite microstructure, composed of AlCrN crystallites embedded in an a-Si_xN_y matrix, also results in a substantial grain refinement. This is reflected by broad peaks with low intensity in the X-ray diffractograms of the Si-containing coatings at RT in Figure 3. Furthermore, the addition of Si to AlCrN shifts the transition between cubic and hexagonal crystal structure to lower Al-contents (Al/Cr ratio is kept constant for all coatings) and thus an additional hexagonal phase forms for AlCrSi_{2.5}N and AlCrSi₅N already during deposition.

During annealing, the first exothermic reaction visible in Figure 2 starts 40 °C above deposition temperature (480 °C) at 520 °C for all coatings and is related to recovery processes of deposition induced lattice defects [32]. This is also reflected by decreasing FWHM with increasing annealing temperatures in Figure 3). Since the cubic AlCrN solid solution is a thermodynamically metastable phase, it decomposes into an Al-rich h-Al(Cr)N and a Cr-rich c-Cr(Al)N phase at elevated temperatures [14]. Nucleation and growth of the h-AlN precipitates starts at grain boundaries [14] and are associated with heat formation reflected by an exothermic contribution to the DSC signal (Figure 2) with a peak maximum at 850 °C. At this temperature, first small fractions of h-AlN precipitates are detected for the AlCrN coating without Si (Figure 3a), and the corresponding peak intensity continuously increases with rising annealing temperature. The same trend is observed for the Si-containing coatings, where, however, the formation of the h-AlN precipitates occurs already at lower annealing temperatures.

At temperatures of about 900 °C, the decomposition of Cr-rich Cr(Al)N regions into Cr₂N and pure nitrogen releasing the coatings results in a decreasing sample mass (Figure 2b) and is accompanied by an endothermic contribution to the DSC signal (Figure 2a). The peak maximum of this endothermic reaction is at 1000 °C for the AlCrN coating without Si and shifted to slightly higher temperatures with increasing Si content (Figure 2a). An overall mass loss of 6 %, 3 % and 2 % at 1200 °C for

AlCrN, AlCrSi_{2.5}N and AlCrSi₅N, respectively, indicates that the amount of formed Cr₂N decreases with increasing Si content. The retarded decomposition of the Si-containing coatings is also reflected in the X-ray diffractograms in Figure 3. While the first Cr₂N diffraction peaks at 2θ angles of 42.6° and 43.4° can be seen for the powders annealed at 950 °C for AlCrN and AlCrSi_{2.5}N, they appear at 1000 °C for AlCrSi₅N. Additionally, the intensity of the Cr₂N signal is much lower for AlCrSi₅N compared to the AlCrSi_{2.5}N coatings with 2.5 at.% and without Si.

A changing slope of the mass signal of the AlCrN coating without Si at about 1140 °C (Figure 2b) marks the onset of the decomposition of Cr₂N into Cr and N₂, which is accompanied by an exothermic contribution to the DSC signal (Figure 2a). While decomposition of Cr₂N is observed at 1250 °C in the case of AlCrSi_{2.5}N, it decomposes already at 1200 °C for AlCrSi₅N. Simultaneously with the kink in the mass signals, a considerably strong (compared to AlCrN) endothermic peak appears in the DSC scans. The substantial mass loss and the large endothermic reaction of the Si containing coatings originates from the decomposition of Si_xN_y, which significantly contributes to the heat-flow. Although pure Si₃N₄ is thermally stable up to 1900 °C, it reacts in the presence of Cr forming Cr₃Si at temperatures considerably below 1300 °C [33].

The decomposition of Cr₂N is also indicated by XRD, where a Cr peak ($2\theta \sim 44.1^\circ$) emanates at the expense of the Cr₂N peaks (Figure 3). The first evidence for Cr can be seen at 1200 °C for the AlCrN coating and at 1280 °C for AlCrSi₅N and AlCrSi_{2.5}N, in each case at temperatures slightly above the kink in the mass signal of the TG measurements. Simultaneously with the rising Cr and diminishing Cr₂N reflections an additional peak at 39.5° develops with increasing annealing temperature, which stems from the Cr₃Si phase formed in both Si containing coatings. Since there is more Si disposed in the AlCrSi₅N coating, the amount of formed Cr₃Si phase is higher than that for AlCrSi_{2.5}N, resulting in a higher intensity of the Cr₃Si peak.

The constant sample mass and a constant heat flow at temperatures above 1400 °C indicate fully completed structural changes. The X-ray diffractograms of the coating powders measured after the DSC experiments (orange lines in Figure 3 at 1450 °C) reveal exclusively h-Al(Cr)N and Cr, plus the Cr₃Si phase in the case of the Si-containing coatings. High peak intensities and small FWHM indicate a microstructure with less lattice defects and significant coarser grain structure after annealing [14].

3.3.2. In-situ high-temperature high-energy grazing-incidence transmission X-ray diffraction

DSC and TG measurements typically provide information about exothermic and endothermic reactions and decomposition processes of materials at dedicated temperatures during annealing. The methods are commonly limited to the use of powdered samples to get a sufficient signal from the coating when analysing coated samples. Furthermore, complementary investigations such as ex-situ XRD are often necessary to obtain a deeper understanding of the ongoing processes and structural

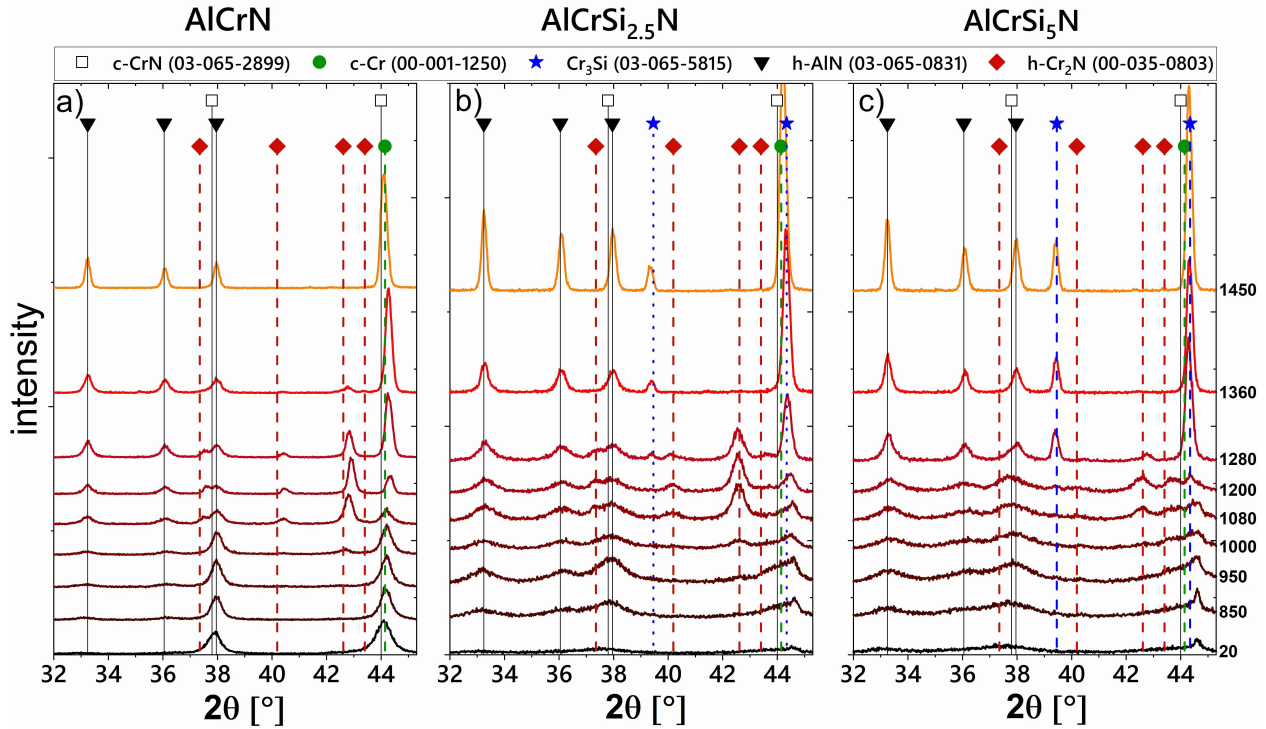


Figure 3: X-ray diffractograms of (a) AlCrN, (b) AlCrSi_{2.5}N and (c) AlCrSi₅N coatings in the as-deposited state and after annealing at various temperatures in Ar atmosphere. A zoom-in from 42° to 45.5° is shown in Supplementary Figure A.1 to show more details.

changes during annealing. On the contrary, in-situ HT-HE-GIT-XRD using a 400 $\mu\text{m} \times 100 \mu\text{m}$ X-ray beam in transmission geometry facilitates a structural analysis of coated samples with the possibility to separate the signals from coating and substrate. The main advantage of this method arises from the capability to analyse the whole coating-substrate system in contrast to the investigation of powdered samples. For the latter case, the coatings are strongly affected by the sample preparation, as residual stress relaxes during powdering and grinding. The impact of stress release due to sample preparation will be discussed in more details in section 4. Furthermore, in-situ HT-HE-GIT-XRD allows for determination of numerous independent material characteristics of coating and substrate and their variation as a function of annealing temperature such as phase composition, FWHM, texture, intrinsic and thermal residual stress components and thermal expansion coefficients.

The phase evolution of the coatings during annealing is shown in Figure 4. Besides reflections emanating from the coating, corresponding to h-Al(Cr)N, c-Cr(Al)N and h-Cr₂N, also WC and Co reflections stemming from the substrate are visible. A slight peak shift to lower angles with increasing temperature and back to higher angles with decreasing temperature corresponds to the changing lattice parameter attributed to the thermal expansion. Especially the position of the Co peak strongly varies with the annealing temperature due to the metallic nature of Co and its greater thermal expansion coefficient with respect to the other phases.

The diffraction patterns in the as-deposited state of all coatings on the cemented carbide substrates (inserted in Figure 4) match with those of the powdered samples in Figure 3. They

only differ concerning the WC and Co substrate peaks at 3.25° and 3.95°, respectively, present only in the measured spectra of coated samples in Figure 4. While the AlCrN coating consists of exclusively cubic phase in the as-deposited state, the Si-containing coatings exhibit a dual-phase crystallographic structure comprising of c-Cr(Al)N and h-Al(Cr)N. Furthermore, a much finer grain size of the Si containing coatings is reflected by very broad peaks (also resulting in a brighter appearance of the phase plots in Figure 4b and c, while maintaining the same colour-scaling compared to Figure 4a). The texture development of the coatings with the annealing temperature is shown in Figure A.2. While the single-phase cubic crystal structure of AlCrN exhibits a (111) fibre texture, the cubic crystallites of the dual-phase Si-containing coatings are predominantly (110)-oriented, and the hexagonal crystallites exhibit a (110) fibre texture too. The crystallites of the h-Al(Cr)N formed during annealing of AlCrN exhibit a less pronounced texture.

The Si-free c-AlCrN coating starts to decompose into h-Al(Cr)N and c-Cr(Al)N at about 750 °C. The further decomposition of the Cr-enriched c-Cr(Al)N into Cr₂N is evidenced by additional reflexes at 3.6° and 3.8°. While the first Cr₂N peaks arise at 1050 °C for AlCrN, Cr₂N formation is retarded to 1100 °C for AlCrSi_{2.5}N. Finally, the formation of Cr₂N is completely suppressed within the measured temperature range with a maximum of 1100 °C for the AlCrSi₅N coating. Interestingly, despite the multiple phase decomposition, the orientation of the cubic and hexagonal crystallites has not changed during annealing (Figure A.2).

Since the FWHM of X-ray diffraction peaks is generally sensitive to the presence of lattice defects, size of coherently

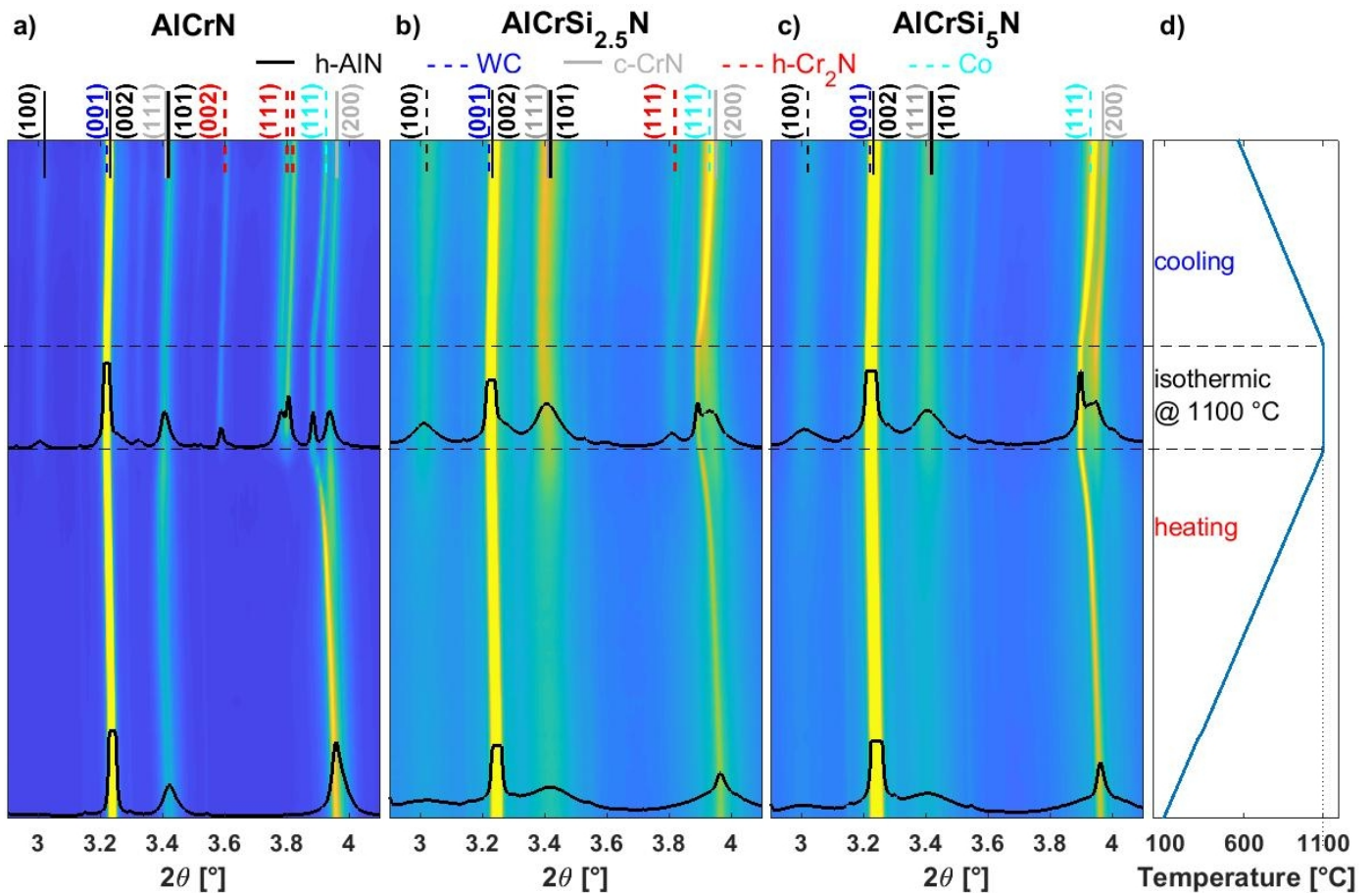


Figure 4: Diffraction intensities $I(\theta, T)$ along the annealing temperature showing the development of the crystallographic structure of the (a) AlCrN, (b) AlCrSi_{2.5}N and (c) AlCrSi₅N coating, together with (d) the applied temperature including heating from RT to 1100 °C with 10 K min⁻¹, isothermal holding at 1100 °C for 5 min and cooling back to RT with 10 K min⁻¹. Diffractograms of each coating at RT and at 1100 °C are inserted for ancillary visualization.

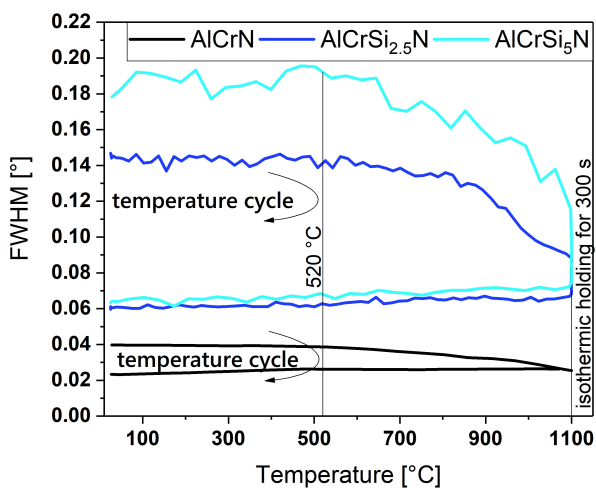


Figure 5: Development of the FWHM as a function of annealing temperature. The values were assessed from the representative CrN(111) peak having the highest intensity without an overlap with any reflection from the substrate.

diffracting domains and micro-strains of second and third order, the FWHM values plotted in Figure 5 thus reflect the temperature-dependent variations of structural defect densities

and grain sizes of the corresponding coatings. The FWHM were evaluated by fitting the CrN (111) diffraction peaks using the Pseudo-Voigt function. The higher scattering in the FWHM of the Si-containing coatings (Figure 5) originated from the fitting of the generally broader diffraction peaks with respect to AlCrN and a partial overlap with the Co-peaks stemming from the substrate (Figure 4). Due to the typical columnar growth of crystallites in physical vapour deposition (PVD) coatings in the normal direction with respect to the substrate surface, the evaluation of the Debye-Scherrer rings is restricted to a corresponding range of $\delta = \pm 10^\circ$ around the out-of-plane diffraction vector (for better understanding see Figure 1 in [1]). Thus, only crystal planes oriented approximately parallel to the surface contribute to the evaluated signal, which allows concluding particularly about the elongation of the grains in growth direction.

The analysis of the FWHM of the dominant reflections of the coatings in Figure 5 reveals its increase with an increasing Si. The encapsulation of the grains by the Si_xN_y tissue limited the grain growth resulting in a fine-grained nano-composite structure, compared to the larger grains developing during the columnar grain growth of AlCrN without Si (also seen in Figure 1). Almost no variation of the FWHM up to tem-

peratures slightly above the deposition temperature at 520 °C further reflects stability of the microstructure of all coatings in terms of process-induced lattice defects and grain size in this temperature range. Above this temperature, recovery processes and possible grain growth are observed as indicated by continuously decreasing FWHM. Defect annihilation, grain growth and reduction of micro-strains during annealing occur intensified with increasing Si content in the coatings, reflected by a higher difference of the FWHM between the as-deposited state and after annealing with respect to the Si free coating (Figure 5). The FWHM is reduced by 50 %, 57 % and 67 % for AlCrN, AlCrSi_{2.5}N and AlCrSi₅N, respectively. This may most probably be due to a higher driving force for structural changes because of the smaller grain size and a higher defect density of the initial state of the nano-composite structure.

For the AlCrN coating, the FWHM does not change during the isothermal holding segment at the maximum temperature of 1100 °C. This documents no further ongoing defect annihilation or grain growth occurring at that temperature. On the contrary, both Si-containing coatings exhibit decreasing FWHM during the isothermal holding segment, which indicates a sufficiently high driving force for ongoing recovery processes and possible grain growth of the crystallites of the nano-composite structure. Lower thermal stability of the microstructure in terms of defect annihilation is observed for AlCrSi₅N compared to AlCrSi_{2.5}N. The FWHM of all coatings remains constant between 1100 °C and RT, indicating no further structural changes during cooling (Figure 5).

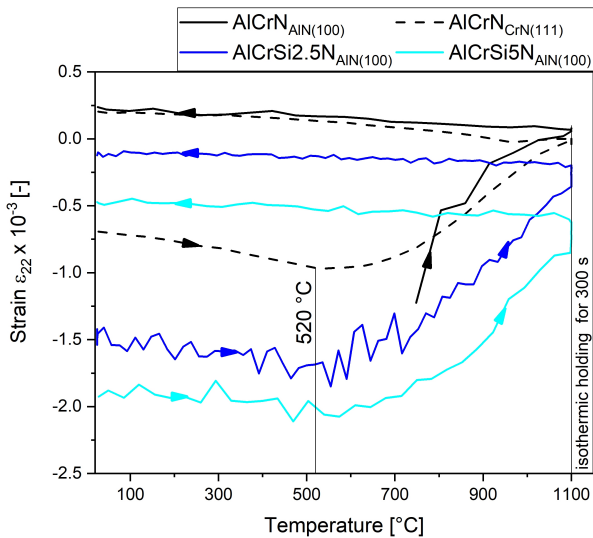


Figure 6: Development of the in-plane residual strains along annealing temperature. The strains were evaluated from the h-AlN (100) peak of the particular coatings. Since there is no hexagonal phase for the AlCrN coating without Si up to 750 °C, strains evaluated from the c-CrN (111) peak are presented additionally. Note, that the Si-containing coatings obtain more scattering, which can again be referred to the broader diffraction peaks (Figure 4).

The evolution of in-plane elastic residual strain as a function of temperature is shown in Figure 6. The strain for all coatings is obtained by evaluating the ellipticity of the corresponding h-AlN (100) Debye-Scherrer rings, which were chosen as

they are less overlapping with a diffraction signal stemming either from the cubic AlCrN phase or the substrate. Since AlCrN is composed exclusively of the cubic phase up to 750 °C, the c-CrN (111) ring is additionally evaluated to get information about strain variation for the whole temperature range. (A detailed description of the methodology used for the strain evaluation including the equations used for the calculations is given in [28].)

The evaluation of strains via the ellipticity of the Debye-Scherrer rings provides information about the overall residual strain state comprising of two dominant components: intrinsic and thermal strain. Extrinsic strains stemming from structural misfits between substrate and coating, precipitations and plastic or creep deformation are neglected here, since they play only a minor role compared to the other two components [34].

All coatings exhibit compressive residual strain in the as-deposited state, reflecting formation of a high number of deposition induced lattice defects. The compressive strain increases with increasing Si content from -0.7×10^{-3} for AlCrN to -1.5×10^{-3} for AlCrSi_{2.5}N and -2.0×10^{-3} for AlCrSi₅N. With the supplemental information about the TECs of substrate and coating materials, a statement whether the state of the thermal strain component is tensile or compressive is determined. The TECs, determined from the unstrained lattice parameters of the particular phase (for more detail see [28]), are $5.5 \times 10^{-6} \text{ K}^{-1}$ for the tungsten carbide, and $11.1 \times 10^{-6} \text{ K}^{-1}$ and $6.3 \times 10^{-6} \text{ K}^{-1}$ for the cubic and the hexagonal phase of the coatings, respectively. Because of the smaller TEC of the substrate compared to the coatings, a tensile thermal strain contribution develops for all coatings when the samples are cooled down after deposition to room temperature.

A reduction of the tensile thermal strain contribution leads to an increase of the overall compressive residual strain in the temperature range between RT and 520 °C, as shown in Figure 6. At 520 °C, which is slightly higher than the deposition temperature, lattice defects start to anneal out as indicated by the variation of the FWHM in Figure 5. This results in a reduction of the intrinsic (compressive) strain component leading to a continuous decrease of the overall compressive residual strain [14]. At the maximum temperature of 1100 °C, compressive strain is reduced to -0.3×10^{-3} and -0.8×10^{-3} for AlCrSi_{2.5}N and AlCrSi₅N, respectively, and completely relaxes for Si-free AlCrN.

The strain relaxation of AlCrSi_{2.5}N and AlCrSi₅N continues during the isothermal holding segment at 1100 °C, while the strain state of AlCrN remains unchanged (Figure 6). This can be correlated with the ongoing recovery processes of the Si-containing coatings described above and indicated in Figure 5. As a consequence of the decreased intrinsic (compressive) strain component associated with defect annihilation, the residual strain state after the annealing is determined as -0.2×10^{-3} and -0.5×10^{-3} for AlCrSi_{2.5}N and AlCrSi₅N, respectively, and becomes even tensile for AlCrN with $+0.3 \times 10^{-3}$.

3.4. Hardness and elastic modulus

The hardness and elastic modulus values of the coatings as a function of Si content in the as-deposited state and after vac-

uum annealing at 1100 °C for 30 min are presented in Figure 7. In the as-deposited state, the AlCrN coating exhibits the highest hardness of 32 GPa. The addition of Si into AlCrN is accompanied by a reduction of hardness to about 28 GPa. The elastic modulus follows a similar trend and decreases from 423 GPa for AlCrN to 345 GPa and 333 GPa for AlCrSi_{2.5}N and AlCrSi₅N, respectively. These findings will be discussed in more details in section 4.

The mechanical properties change significantly after vacuum annealing reflecting the structural changes of the coatings. While annealing results in a drop in hardness down to 26 GPa for AlCrN, a slight increase above 29 GPa occurs for both Si containing coatings. The elastic modulus of AlCrN also decreases after annealing to 423 GPa, whereas AlCrSi_{2.5}N and AlCrSi₅N obtain an increase up to ~ 360 GPa.

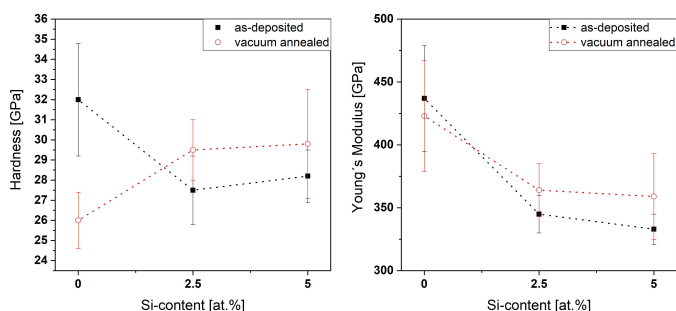


Figure 7: Development of (a) hardness and (b) elastic modulus of the AlCr(Si)N coatings as a function of Si content in the as-deposited state and after vacuum annealing at 1100 °C for 30 min.

4. Discussion

The thermal stability of a material is generally related to changes of its properties at elevated temperatures. In the case of protective hard coatings, the property variations are related to changes in microstructure given by recovery processes, phase transformations, etc. Coatings synthesised by PVD techniques generally grow under conditions far from the thermodynamic equilibrium. The apparent kinetic limitations as a result of rapid cooling at the atomic scale during deposition allow for formation of phases in metastable states and coatings with unique properties, which are otherwise not accessible in their bulk material counterparts. The metastable nature of such materials, however, often limits their application at elevated temperatures, as microstructural changes typically deteriorate their mechanical properties. Since the properties of ceramic hard coatings are mainly governed by their microstructure, a comprehensive understanding of their phase composition, defect density and residual stress state as a function of temperature is required. To analyse the thermal stability of the AlCr(Si)N coatings and its underlying mechanisms (defect recovery, recrystallisation, phase transformations, decomposition, strain relaxation, etc.), a newly developed in-situ HT-HE-GIT-XRD method combined with conventional DSC, TGA and XRD was used for investigation of three AlCr(Si)N coatings with 0 at.%, 2.5 at.% and 5 at.% Si and a fixed Al/Cr atomic ratio of 70/30. While

DSC/TG measurements together with the X-ray diffractograms of coating powders annealed at specific temperatures give detailed information about chemical reactions, phase transitions and decomposition up to a temperature of 1450 °C, the in-situ HT-HE-GIT-XRD method allows to study the whole coating-substrate system (instead of a powdered coating) and to simultaneously access the phase composition, defect density and grain size and residual strain state as a function of temperature up to 1100 °C. By combination of the advanced in-situ HT-HE-GIT-XRD method with conventional DSC/TG, the influence of the residual stress state on the thermal stability of the coatings became accessible, as discussed later in this section.

An effect of Si on the coating microstructure and its properties has been demonstrated for the TiN [35], AlTiN [36], CrN [37] and AlCrN [17] coating systems. Already at small Si contents, a complete change of the coating's microstructure from a columnar grain morphology to a nano-composite structure has been observed. In AlCrSiN, the Si-N bonds are preferred compared to Cr-Si or Al-Si bonds, resulting in a low solubility of Si in AlCrN crystallites and a lower free energy of separated phases in comparison to AlCrSiN compounds [15, 18]. Due to the near-complete immiscibility of MeN_x metal nitride and the Si_xN_y phase, the nano-composite structure forms as a result of spinodal decomposition, comprising of MeN crystallites in an a-Si_xN_y matrix [38–40]. To assure the formation of the nano-composite structure during deposition, a sufficiently high activity of nitrogen and a sufficiently high temperature to allow diffusion during film growth is necessary. The nitrogen pressure of 4 Pa and the deposition temperature of 480 °C meet these conditions stated in [35]. Hence, the formation of a nano-composite microstructure is observed for the AlCrSiN coatings studied in this work, accompanied by a strong decrease in crystallite size, as indicated by large FWHM in Figure 3, Figure 4 and Figure 5, and also corroborated by the glassy and featureless appearance of the fracture cross-sections in Figure 1.

Although theoretical predictions report a critical AlN content of ~ 75 at.% [41] for the formation of the cubic crystal structure, AlCrN coatings composed exclusively of cubic phase were experimentally synthesised by PVD techniques only up to a maximum AlN fraction of 71 at.% [12]. Since the amount of AlN of the coatings analysed in this work is relatively close to this critical AlN content (in the range of 61 at.% to 65 at.%, see Table 1), only the coating without supplemental Si is stabilized in the purely cubic modification (Figure 3 and Figure 4). AlCrSi_{2.5}N and AlCrSi₅N exhibit a dual-phase hexagonal and cubic crystal structure with a similar content of hexagonal phase for both coatings. Since the Al/Cr ratio is constant for all investigated coatings, the formation of the hexagonal phase can be related to the addition of Si with consequential changes in the microstructure (grain size, defect density) and residual stress state. Moreover, former studies have revealed that, besides elemental composition, also compressive stress [42], vacancies [43] and the Al distribution on the metal sublattice [44] affect the formation of a hexagonal phase in the AlCrN or AlTiN systems. Recently, Hans et al. [45] have shown that also surface energy and therefore the crystallite size has a major influence on the phase formation of metastable materials. They calculated stability ranges

for the cubic and hexagonal phases in AlTiN as a function of crystallite size and found that the hexagonal phase becomes favoured for small grain sizes. These findings may also explain the destabilisation of the cubic phase in AlCrN when adding Si, as the encapsulation of the AlCr(Si)N crystallites by the amorphous Si_xN_y tissue results in a considerably grain refinement (Figure 5) with a subsequent increase of the surface energy. If this contribution to the total energy becomes dominant, a stabilisation of the hexagonal phase may be expected. Furthermore, Si affects the character of the chemical bondings in the AlCrN system. Contrary to CrN, where the metallic bonding character dominates, the Si-N bonds have, similarly to Al-N, a strong covalent bonding character. The consequent changes in electronic structure when adding Si to AlCrN go along with the structural transformation from cubic to hexagonal [46].

The incorporation of Si atoms into the AlCrSiN matrix also results in a larger defect density and greater stress of second order with an increasing Si content, indicated by larger FWHM in Figure 5 and higher compressive residual strain in Figure 6. Although a larger number of defects leads to a higher driving force for recovery and thus decreased thermal stability of defects [47], recovery processes for all coatings start at the same temperature of 520 °C, i.e. 40 °C above deposition temperature. The first phase transformation taking place at elevated temperatures is the decomposition of the metastable c-AlCrN phase into h-Al(Cr)N and c-Cr(Al)N. It occurs to a similar extent for all three coatings, with a maximum exothermic contribution to the DSC signal at ~ 850 °C. Since the formation of the hexagonal phase is accompanied by a volume expansion of 26 % [44], the metastable cubic phase can be stabilized by a compressive residual stress state [48]. Once the substrate is removed and a free-standing coating is received (e.g. powdered coating), the compressive residual stresses in the coatings relax and only the intrinsic stresses of second and third order are left. Therefore, the measured properties of a coating on a substrate differ from the measured properties of a free-standing coating, e.g. observed for fracture toughness in [49] or phase stability in [50]. The effect of the state of the coating (coated substrate versus powder) and its resulting residual stress state on the measured material's properties is reflected by the decomposition of CrN into Cr_2N at elevated temperatures. The onset for the decomposition of CrN is observed at higher temperatures for coating-substrate systems than for stress free powders, at 1050 °C compared to 950 °C, at 1100 °C compared to 950 °C and above 1100 °C compared to 1000 °C for AlCrN, AlCrSi_{2.5}N and AlCrSi₅N, respectively. As synchrotron radiation provides an X-ray beam with high brilliance and thus superior signal-to-noise ratio and much better detection limit for small amounts of phases compared to a conventional XRD, it can be expected that the difference in the onset temperature of decomposition is even higher and the impact of the relaxed stresses is underestimated.

Furthermore, the decomposition of CrN into Cr_2N in the AlCrN-based systems, accompanied by a release of nitrogen, is critical for the behaviour of the coatings at elevated temperatures, since the associated formation of pores deteriorate the mechanical properties. Here, a positive impact of Si becomes

evident since the onset temperature is retarded to higher temperatures and the decomposition is decelerated with increasing Si content (Figure 2 and Figure 4). The impeded formation of Cr_2N can be attributed to the nano-composite structure of the AlCrSiN coatings, where the AlCr(Si)N crystals are embedded by the dense Si_xN_y tissue, which restricts the segregation of atoms to small distances within the separated nano-grains [24]. Similar to the prohibited diffusion of oxygen in AlTiN coatings alloyed with yttrium [51] or nc-TiN/a- Si_xN_y coatings [52] during oxidation, the strong and dense interface of the a- Si_xN_y hinders diffusion of nitrogen along the grain boundaries. Therefore, nitrogen can not be released from the crystal when CrN decomposes into Cr_2N , which effectively suppresses the further decomposition of CrN.

As a final step, Cr_2N starts to decompose at 1140 °C for AlCrN and, at 1280 °C and 1200 °C for AlCrSi_{2.5}N and AlCrSi₅N, respectively. The decomposition of Cr_2N is accompanied by the decomposition of Si_xN_y in the case of the Si containing coatings. Although the amount of Si in both Si containing coatings is relatively low, the endothermic peaks above 1200 °C are considerably high compared to AlCrN and all other reactions occurring during annealing (Figure 2). This is due to the superimposed contribution to the DSC signal of the decomposition reactions of Cr_2N and Si_xN_y . Additionally, the large enthalpy of formation of $\Delta H_{\text{Si}_x\text{N}_y}^0 = -760 \text{ kJ mol}^{-1}$ [53] compared to $\Delta H_{\text{CrN}}^0 = -123 \text{ kJ mol}^{-1}$ [54] and $\Delta H_{\text{Cr}_2\text{N}}^0 = -234 \text{ kJ mol}^{-1}$ [55] results in a considerably high endothermic heat flow when it decomposed.

Besides the thermal stability of the microstructure, the associated evolution of mechanical properties as a function of temperature is of major importance for the functionality of coatings at elevated temperatures. Obtaining a remarkable high hardness of ceramic hard coatings, representing a key property determining together with elastic modulus its wear resistance, can be approached by: (i) selecting materials with intrinsically high hardness (e.g. diamond, hydrogen-free diamond-like carbon, cubic boron nitride); (ii) the effect of ion bombardment during deposition; and (iii) microstructural design of coatings with heterogeneous microstructure such as nano-composites [39]. While a hardness enhancement by energetic ion bombardment is associated with a decrease in crystallite size, densification and the generation of high defect densities accompanied by the development of compressive residual stress, enhanced hardness of nanostructured materials is a result of hindered dislocation movement among fine-grained constituents with different lattice structures [47]. The high hardness of coatings obtained by an intense ion bombardment during deposition is typically not maintained at temperatures significantly above deposition temperature, since recovery effects lead to a reduction of compressive residual stress. Contrary, the high hardness of nano-composite materials can be preserved to temperatures above 1000 °C [56], as crystallite growth is suppressed by the amorphous tissue embedding the nano-crystallites. Within the AlTiN and AlCrN systems, many attempts have been made to stabilize the material in its cubic configuration [12, 57, 58] due to the enhanced mechanical properties compared to its hexagonal con-

figuration. Although the cubic modification may be favoured in terms of mechanical properties for applications at moderate temperatures, considerable constraints may arise from its metastable nature at elevated temperatures, as hardness drops with the formation of hexagonal phase fractions.

In the case of the AlCr(Si)N coatings studied in this work, the hardness at room temperature and after annealing can be attributed to (i) the formed phases, (ii) the amount of residual stress and (iii) the microstructural design focused on the formation of a nano-composite. At room temperature, AlCrN exhibits the highest hardness, since it is the only coating with purely cubic phase. The reduced hardness of the Si-containing coatings is mainly related to the formation of an additional hexagonal phase. Neither the nano-composite structure (and thus smaller grain size), nor the increased compressive residual strain can compensate the loss of hardness resulting from the formation of larger fractions of the much softer hexagonal phase. However, the advantage of Si as an alloying element in the AlCrN system becomes evident while looking at the hardness development of the coatings after vacuum annealing at 1100 °C. While AlCrN without Si suffers from a large drop in hardness of 5 GPa, mainly due to the phase transformation of the metastable cubic into the thermodynamically more stable hexagonal phase (Figure 3a and Figure 4) and a simultaneous reduction of the compressive residual strain towards slight tensile strain (Figure 6), the hardness of both Si-containing coatings increases of about 2 GPa after annealing. Similar to AlCrN, lattice defects and compressive residual strain are not stable above deposition temperature and vanish to a large extent (Figure 5 and Figure 6). Therefore, the stabilized (or even increasing) hardness can be related to the nano-composite microstructure, where mainly two processes should be considered as an explanation for the increase after annealing. At first, an incomplete phase segregation during deposition is completed upon annealing [39]. Secondly, additional hexagonal AlN precipitates form during annealing, accompanied by coherency strains hindering plastic deformation with a subsequent increase in hardness [9]. While the coherency strains in single-phase AlCrN contribute to age hardening limited to a maximum in hardness at 700 °C [9], the enhanced hardness of AlCrSi_{2.5}N and AlCrSi₅N in this work is still observed at 1100 °C. Finally, the suppressed formation of Cr₂N in the Si-containing coatings (accompanied by the release of nitrogen and the formation of pores) to temperatures above 1100 °C is an important factor to preserve the hardness. Summarized, while a single-phase cubic crystal structure seems beneficial in terms of mechanical properties at a first glance, the nano-composite and dual-phase cubic and hexagonal structure outperforms its mono-phase counterparts at elevated temperatures and makes the AlCrSiN coatings studied in this work promising candidates for high-temperature applications.

5. Summary and Conclusions

Three arc evaporated coatings, AlCrN, AlCrSi_{2.5}N and AlCrSi₅N, were investigated and the impact of Si on (i) the phase formation, (ii) thermal stability and (iii) mechanical properties as a function of temperature was studied. Using

the novel in-situ HT-HE-GIT-XRD allowed for measuring the temperature-dependent variations of the coating microstructure of the coating on a substrate (in contrast to powdered coatings). The unique combination of the in-situ HT-HE-GIT-XRD method with conventional DSC and TG revealed a significant impact of sample preparation in stress-free powders, resulting in a 100 °C lower onset temperature of the decomposition of CrN into Cr₂N when measuring powdered samples compared to the coating-substrate systems. The addition of Si resulted in the formation of (i) a nano-composite and (ii) dual-phase cubic and hexagonal structure with enhanced thermal stability and improved mechanical properties at elevated temperatures. This is evident by the shift of the onset temperature for the decomposition of CrN into Cr₂N of 100 °C, related to encapsulated AlCr(Si)N crystals in an a-Si_xN_y tissue phase, where nitrogen diffusion is suppressed. Furthermore, the dual-phase crystal structure reveals its benefits at elevated temperatures, since the hardness of the Si containing coatings increased by ~ 2 GPa to almost 30 GPa after annealing at 1100 °C, while the hardness of AlCrN dropped from 32 GPa to 26 GPa. The hardness increase after annealing is related to a thermally much more stable nano-composite structure (suppressed grain growth) with hindered dislocation movement due to the a-Si_xN_y tissue phase, and to age hardening effects of a dual-phase cubic and hexagonal structure at temperatures above 1100 °C. The findings emphasize the potential of Si as an eminently suitable alloying element to enhance the thermal stability of the AlCrN system. The formation of a nano-composite structure, consisting of dual-phase cubic and hexagonal crystallites embedded in an a-Si_xN_y tissue, and the enhanced mechanical properties at elevated temperatures make the AlCrSiN coatings promising candidates for high-temperature applications.

6. Acknowledgements

The work has been financially supported by Christian Doppler Research Association. The financial support by the Austrian Federal Ministry for Digital and Economic Affairs and the National Foundation for Research, Technology and Development is gratefully acknowledged.

References

- [1] J. Keckes, R. Daniel, J. Todt, J. Zalesak, B. Sartory, S. Braun, J. Gluch, M. Rosenthal, M. Burghammer, C. Mitterer, et al. 30 nm X-ray focusing correlates oscillatory stress, texture and structural defect gradients across multilayered TiN-SiO_x thin film. *Acta Materialia*, 144:862–873, 2018.
- [2] J. Zalesak, M. Bartosik, R. Daniel, C. Mitterer, C. Krywka, D. Kiener, PH. Mayrhofer, and J. Keckes. Cross-sectional structure-property relationship in a graded nanocrystalline Ti1-xAlxN thin film. *Acta Materialia*, 102:212–219, 2016.
- [3] R. Daniel, M. Meindlhumer, W. Baumegeger, J. Zalesak, B. Sartory, M. Burghammer, C. Mitterer, and J. Keckes. Grain boundary design of thin films: using tilted brittle interfaces for multiple crack deflection toughening. *Acta Materialia*, 122:130–137, 2017.
- [4] S. Klima, N. Jäger, H. Hruby, C. Mitterer, J.F. Keckes, M. Burghammer, and R. Daniel. Structure-stress relationships in nanocrystalline multilayered Al_{0.7}Cr_{0.3}N/Al_{0.9}Cr_{0.1}N coatings studied by cross-sectional X-ray nanodiffraction. *Materials & Design*, 170:107702, 2019.

- [5] N. Jäger, S. Klima, H. Hruby, J. Julin, M. Burghammer, J.F. Keckes, C. Mitterer, and R. Daniel. Evolution of structure and residual stress of a fcc/hex-AlCrN multi-layered system upon thermal loading revealed by cross-sectional X-ray nano-diffraction. *Acta Materialia*, 162:55 – 66, 2019.
- [6] G. List, G. Sutter, and A. Bouthiche. Cutting temperature prediction in high speed machining by numerical modelling of chip formation and its dependence with crater wear. *International Journal of Machine Tools and Manufacture*, 54-55:1–9, 2012.
- [7] U. Schleinkofer, C. Czettl, and C. Michotte. Coating Applications for Cutting Tools. In *Comprehensive Hard Materials*, pages 453–469. Elsevier, 2014.
- [8] C. Mitterer. PVD and CVD Hard Coatings. In *Comprehensive Hard Materials*, pages 449–467. Elsevier, 2014.
- [9] H. Willmann, P. H. Mayrhofer, L. Hultman, and C. Mitterer. Hardness evolution of Al–Cr–N coatings under thermal load. *Journal of Materials Research*, 23(11):2880–2885, 2008.
- [10] H. Willmann, P. H. Mayrhofer, L. Hultman, and C. Mitterer. Thermal stability and age hardening of supersaturated AlCrN hard coatings. *International Heat Treatment and Surface Engineering*, 1(2):75–79, 2013.
- [11] C. Sabitzer, J. Paulitsch, S. Kolozsvári, R. Rachbauer, and P. H. Mayrhofer. Influence of bias potential and layer arrangement on structure and mechanical properties of arc evaporated Al–Cr–N coatings. *Vacuum*, 106:49–52, 2014.
- [12] A. E. Reiter, V. H. Derflinger, B. Hanselmann, T. Bachmann, and B. Sartory. Investigation of the properties of Al_{1-x}Cr_xN coatings prepared by cathodic arc evaporation. *Surface and Coatings Technology*, 200(7):2114–2122, 2005.
- [13] M. Kawate, A. Kimura, and T. Suzuki. Microhardness and lattice parameter of Cr_{1-x}Al_xN films. *Journal of Vacuum Science & Technology A: Vacuum, Surfaces, and Films*, 20(2):569–571, 2002.
- [14] H. Willmann, P. H. Mayrhofer, P.O.Å. Persson, A. E. Reiter, L. Hultman, and C. Mitterer. Thermal stability of Al–Cr–N hard coatings. *Scripta Materialia*, 54(11):1847–1851, 2006.
- [15] J. Soldán, J. Neidhardt, B. Sartory, R. Kaindl, R. Čerstvý, P. H. Mayrhofer, R. Tessadri, P. Polcik, M. Lechthaler, and C. Mitterer. Structure–property relations of arc-evaporated Al–Cr–Si–N coatings. *Surface and Coatings Technology*, 202(15):3555–3562, 2008.
- [16] T. Polcar, T. Vitu, J. Sondor, and A. Cavaleiro. Tribological Performance of CrAlSiN Coatings at High Temperatures. *Plasma Processes and Polymers*, 6(S1):S935–S940, 2009.
- [17] C. Trittemmel, R. Daniel, M. Lechthaler, P. Polcik, and C. Mitterer. Influence of Al and Si content on structure and mechanical properties of arc evaporated Al–Cr–Si–N thin films. *Thin Solid Films*, 534:403–409, 2013.
- [18] J. L. Endrino, S. Palacín, A. Gutiérrez, F. Schäffers, and J. E. Krzanowski. Low and increased solubility of silicon in metal nitrides: Evidence by X-ray absorption near edge structure. *J Mater Sci*, 42(17):7607–7610, 2007.
- [19] S. Veprek and M. Jilek. Super- and ultrahard nanocomposite coatings: generic concept for their preparation, properties and industrial applications. *Vacuum*, 67:443–449, 2002.
- [20] L. Castaldi, D. Kurapov, A. Reiter, V. Shklover, P. Schwaller, and J. Patscheider. High temperature phase changes and oxidation behavior of Cr–Si–N coatings. *Surface and Coatings Technology*, 202(4-7):781–785, 2007.
- [21] J. Musil, R. Daniel, J. Soldán, and P. Zeman. Properties of reactively sputtered W–Si–N films. *Surface and Coatings Technology*, 200(12-13):3886–3895, 2006.
- [22] K. Lukaszkoicz, K. Labisz, M. Basiaga, and E. Jonda. Nano-Scale Structure Investigation of Vapour Deposited AlCrSiN Coating Using Transmission Electron Microscope Techniques. *Archives of Metallurgy and Materials*, 61(2):837–842, 2016.
- [23] W. Wu, W. Chen, Shubao Yang, Y. Lin, S. Zhang, T. Cho, G. H. Lee, and S. Kwon. Design of AlCrSiN multilayers and nanocomposite coating for HSS cutting tools. *Applied Surface Science*, 351:803–810, 2015.
- [24] S. Veprek, H.-D. Männling, M. Jilek, and P. Holubar. Avoiding the high-temperature decomposition and softening of (Al_{1-x}Ti_x)N coatings by the formation of stable superhard nc-(Al_{1-x}Ti_x)N/a-Si₃N₄ nanocomposite. *Materials Science and Engineering: A*, 366(1):202–205, 2004.
- [25] T. Polcar and A. Cavaleiro. High temperature properties of CrAlN, CrAlSiN and AlCrSiN coatings – Structure and oxidation. *Materials Chemistry and Physics*, 129(1-2):195–201, 2011.
- [26] T. Vopát, M. Haršáni, M. Kuruc, V. Šimna, R. Zaujec, J. Peterka, and L. Čaplovič. Effect of Substrate Bias and Coating Thickness on the Properties of nc-AlCrN/a-SixNy Hard Coating and Determination of Cutting Parameters. In *Solid State Phenomena*, volume 261, pages 229–236. Trans Tech Publ, 2017.
- [27] M. Meindlhumer, J. Zalesak, R. Pitonak, J. Todt, B. Sartory, M. Burghammer, A. Stark, N. Schell, R. Daniel, J. F. Keckes, et al. Biomimetic hard and tough nanoceramic Ti–Al–N film with self-assembled six-level hierarchy. *Nanoscale*, 2019.
- [28] M. Meindlhumer, S. Klima, N. Jäger, A. Stark, H. Hruby, C. Mitterer, J. Keckes, and R. Daniel. Stress-controlled decomposition routes in cubic AlCrN films assessed by in-situ high-temperature high-energy grazing incidence transmission X-ray diffraction. *Scientific Reports*, 9(1):18027, December 2019.
- [29] A. P. Hammersley, S. O. Svensson, M. Hanfland, A. N. Fitch, and D. Hausermann. Two-dimensional detector software: From real detector to idealised image or two-theta scan. *High Pressure Research*, 14(4-6):235–248, 1996.
- [30] J. Kieffer and D. Karkoulis. PyFAI, a versatile library for azimuthal re-grouping. *Journal of Physics: Conference Series*, 425(20):202012, 2013.
- [31] W.C. Oliver and G.M. Pharr. Measurement of hardness and elastic modulus by instrumented indentation: Advances in understanding and refinements to methodology. *J. Mater. Res.*, 2004(19):3–20, 2004.
- [32] A. Hörling, L. Hultman, M. Odén, J. Sjöln, and L. Karlsson. Thermal stability of arc evaporated high aluminum-content Ti_{1-x}Al_xN thin films. *Journal of Vacuum Science & Technology A: Vacuum, Surfaces, and Films*, 20(5):1815–1823, 2002.
- [33] T. Shimoo and K. Okamura. Interaction of Si₃N₄ with Cr. *Journal of Materials Science*, 1994(29):2231–2237, 1994.
- [34] R. Daniel, J. Keckes, I. Matko, M. Burghammer, and C. Mitterer. Origins of microstructure and stress gradients in nanocrystalline thin films: The role of growth parameters and self-organization. *Acta Materialia*, 61(16):6255–6266, 2013.
- [35] S. Vepřek. The search for novel, superhard materials. *Journal of Vacuum Science & Technology A: Vacuum, Surfaces, and Films*, 17(5):2401–2420, sep 1999.
- [36] S. Q. Wang, L. Chen, B. Yang, K. K. Chang, Y. Du, J. Li, and T. Gang. Effect of Si addition on microstructure and mechanical properties of Ti–Al–N coating. *International Journal of Refractory Metals and Hard Materials*, 28(5):593–596, sep 2010.
- [37] E. Martínez, R. Sanjinés, A. Karimi, J. Esteve, and F. Lévy. Mechanical properties of nanocomposite and multilayered Cr–Si–N sputtered thin films. *Surface and Coatings Technology*, 180-181:570–574, mar 2004.
- [38] J. Patscheider. Nanocomposite hard coatings for wear protection. *MRS bulletin*, 28(3):180–183, 2003.
- [39] S. Veprek, M. GJ Veprek-Heijman, P. Karvankova, and J. Prochazka. Different approaches to superhard coatings and nanocomposites. *Thin solid films*, 476(1):1–29, 2005.
- [40] J. Musil, J. Vlček, and P. Zeman. Hard amorphous nanocomposite coatings with oxidation resistance above 1000°C. *Advances in Applied Ceramics*, 107(3):148–154, may 2008.
- [41] P.H. Mayrhofer, D. Music, Th. Reeswinkel, H.-G. Fuß, and J.M. Schneider. Structure, elastic properties and phase stability of Cr_{1-x}Al_xN. *Acta Materialia*, 56(11):2469–2475, jun 2008.
- [42] D. Holec, F. Florian Rovere, P. H. Mayrhofer, and P. B. Barna. Pressure-dependent stability of cubic and wurtzite phases within the TiN–AlN and CrN–AlN systems. *Scripta Materialia*, 62(6):349–352, mar 2010.
- [43] H. Euchner and P.H. Mayrhofer. Vacancy-dependent stability of cubic and wurtzite Ti_{1-x}Al_xN. *Surface and Coatings Technology*, 275:214–218, aug 2015.
- [44] P. H. Mayrhofer, D. Music, and J. M. Schneider. Influence of the Al distribution on the structure, elastic properties, and phase stability of supersaturated Ti_{1-x}Al_xN. *Journal of Applied Physics*, 100(9):094906, nov 2006.
- [45] M. Hans, D. Music, Y. Chen, L. Patterer, A. O. Eriksson, D. Kurapov, J. Ramm, M. Arndt, H. Rudigier, and J. M. Schneider. Crystallite size-dependent metastable phase formation of TiAlN coatings. *Scientific Reports*, 7(1):16096, November 2017.
- [46] P.H. Mayrhofer, R. Rachbauer, D. Holec, F. Rovere, and J.M. Schneider. Protective Transition Metal Nitride Coatings. In *Comprehensive Materials Processing*, pages 355–388. Elsevier, 2014.

- [47] C Mitterer, P.H Mayrhofer, and J Musil. Thermal stability of PVD hard coatings. *Vacuum*, 71(1-2):279–284, may 2003.
- [48] M. Bartosik, R. Daniel, Z. Zhang, M. Deluca, W. Ecker, M. Stefanelli, M. Klaus, C. Genzel, C. Mitterer, and J. Keckes. Lateral gradients of phases, residual stress and hardness in a laser heated Ti_{0.52}Al_{0.48}N coating on hard metal. *Surface and Coatings Technology*, 206(22):4502 – 4510, 2012.
- [49] M Bartosik, C Rumeau, R Hahn, ZL Zhang, and PH Mayrhofer. Fracture toughness and structural evolution in the TiAlN system upon annealing. *Scientific reports*, 7(1):16476, 2017.
- [50] N. Schalk, C. Mitterer, J. Keckes, M. Penoy, and C. Michotte. Influence of residual stresses and grain size on the spinodal decomposition of metastable Ti_{1-x}Al_xN coatings. *Surface and Coatings Technology*, 209:190 – 196, 2012.
- [51] LA. Donohue, DB. Lewis, WD. Münz, MM. Stack, SB. Lyon, HW. Wang, and D. Rafaja. The influence of low concentrations of chromium and yttrium on the oxidation behaviour, residual stress and corrosion performance of TiAlN hard coatings on steel substrates. *Vacuum*, 55(2):109–114, 1999.
- [52] J. Musil and P. Zeman. Hard a-Si₃N₄/MeN_x Nanocomposite Coatings with High Thermal Stability and High Oxidation Resistance. *Solid State Phenomena*, 127:31–36, sep 2007.
- [53] I. Tomaszewicz. Thermodynamics of Silicon Nitride. Standard molar enthalpy of formation of amorphous Si₃N₄ at 298.15 K. *Journal of Thermal Analysis and Calorimetry*, 65(2):425–433, 2001.
- [54] S. Hofmann and H. A. Jehn. Oxidation behavior of CrN_x and (Cr,Al)N_x hard coatings. *Werkstoffe und Korrosion*, 41(12):756–760, 1990.
- [55] M. Widenmeyer, E. Meissner, A. Senyshyn, and R. Niewa. On the Formation Mechanism of Chromium Nitrides: An in situ Study. *Zeitschrift für anorganische und allgemeine Chemie*, 640(14):2801–2808, 2014.
- [56] H.-D. Männling, D.S. Patil, K. Moto, M. Jilek, and S. Veprek. Thermal stability of superhard nanocomposite coatings consisting of immiscible nitrides. *Surface and Coatings Technology*, 146-147:263 – 267, 2001. Proceedings of the 28th International Conference on Metallurgic Coatings and Thin Films.
- [57] NE. Christensen and I. Gorczyca. Calculated structural phase transitions of aluminum nitride under pressure. *Physical Review B*, 47(8):4307, 1993.
- [58] M. Schlögl, J. Paulitsch, J. Keckes, and PH. Mayrhofer. Influence of AlN layers on mechanical properties and thermal stability of Cr-based nitride coatings. *Thin Solid Films*, 531:113–118, 2013.

Appendix A. Supplemental Material

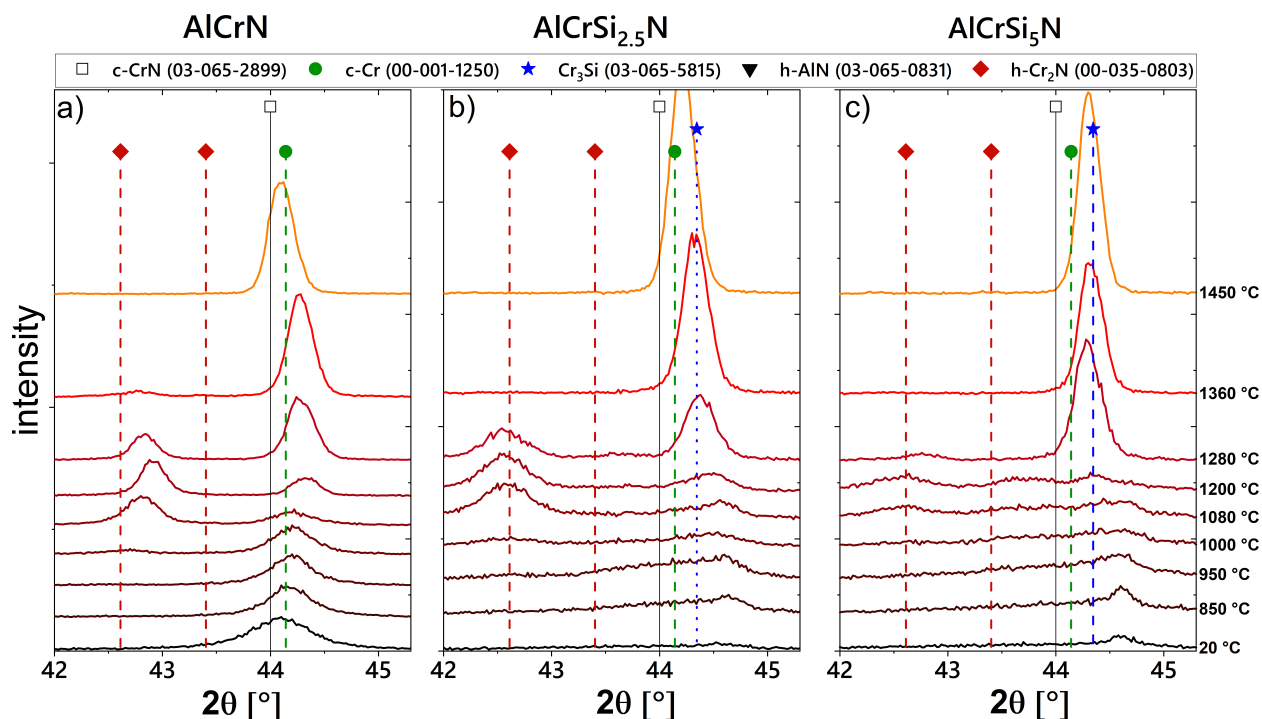


Figure A.1: Detailed view of the X-ray diffractograms in the range from 42° to 45.5° of the (a) AlCrN, (b) AlCrSi_{2.5}N and (c) AlCrSi₅N coatings in the as-deposited state and after annealing at various temperatures in Ar atmosphere.

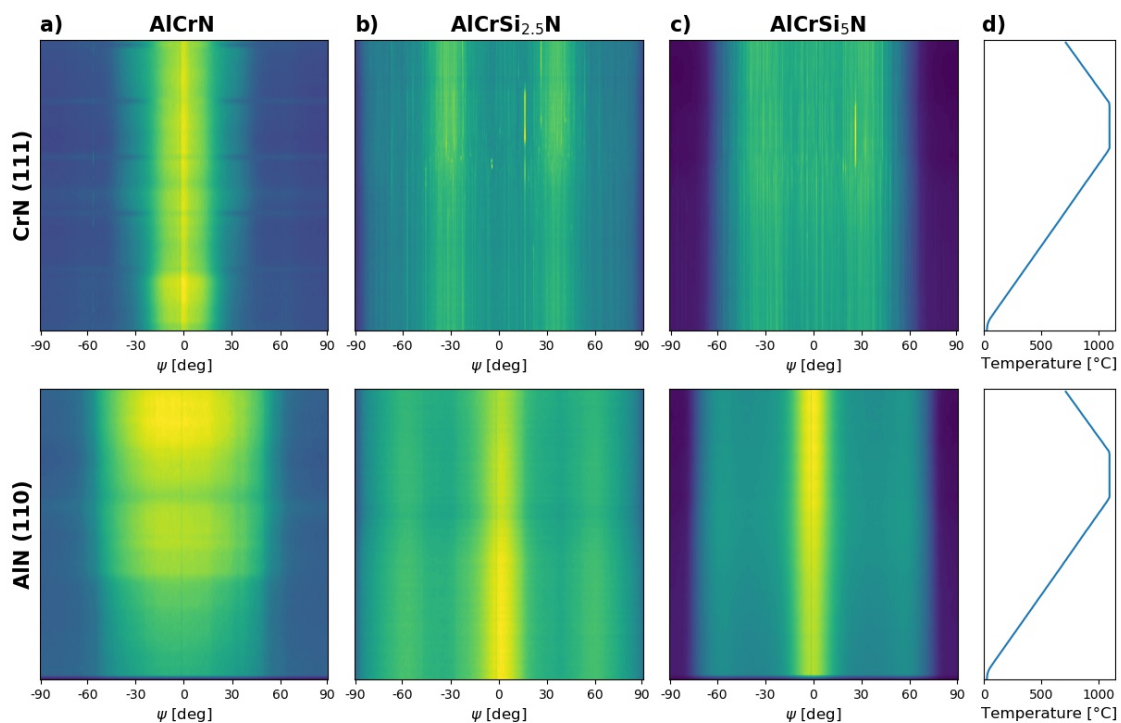


Figure A.2: Intensity of the CrN (111) and the AlN (110) diffractions peaks along the ψ angle as a function of temperature of (a) AlCrN, (b) AlCrSi_{2.5}N and (c) AlCrSi₅N, together with the (d) annealing temperature.